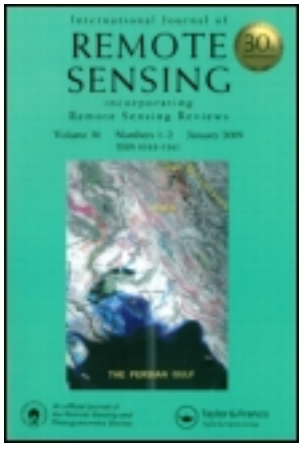

International Journal of Remote Sensing

Publication details, including instructions for authors and subscription information:
http://www.tandfonline.com/loi/tres20

Sea-ice monitoring over the Caspian Sea using geostationary satellite data

Marouane Temimi [a], Peter Romanov [b], Hosni Ghedira [a], Reza Khanbilvardi [a] & Kim Smith [a]

[a] NOAA-CREST, City College / City University of New York, 160 Convent Avenue, New York, NY, 10031, USA

[b] Cooperative Institute for Climate Studies (CICS), University of Maryland, 5825 University Research Court, College Park, MD, 20740, USA

Version of record first published: 15 Feb 2011

To cite this article: Marouane Temimi, Peter Romanov, Hosni Ghedira, Reza Khanbilvardi & Kim Smith (2011): Sea-ice monitoring over the Caspian Sea using geostationary satellite data, International Journal of Remote Sensing, 32:6, 1575-1593

To link to this article: http://dx.doi.org/10.1080/01431160903578820

International Journal of Remote Sensing
Vol. 32, No. 6, 20 March 2011, 1575–1593

Taylor & Francis
Taylor & Francis Group

Sea-ice monitoring over the Caspian Sea using geostationary satellite data

MAROUANE TEMIMI*†, PETER ROMANOV‡, HOSNI GHEDIRA†, REZA KHANBILVARDI† and KIM SMITH†

†NOAA-CREST, City College / City University of New York, 160 Convent Avenue, New York, NY 10031, USA

‡Cooperative Institute for Climate Studies (CICS), University of Maryland, 5825 University Research Court, College Park, MD 20740, USA

(*Received 5 May 2009; in final form 21 December 2009*)

A new technique is proposed for sea-ice mapping using observations from geostationary satellite over the Caspian Sea. A two end-member linear-mixture approach has been employed. A neural-network-based approach was used to simulate water and ice reflectances for all possible sun–satellite geometries. The ice-mapping technique incorporates an advanced cloud-detection algorithm with adaptive threshold values. The average percentage of cloud reduction because of the daily compositing ranged from 22% to 25%. Daily maps of ice distribution and concentration with minimal cloud coverage were produced for the winter seasons of 2007 and 2008. The retrieved ice distribution demonstrated a good agreement with Moderate Resolution Imaging Spectroradiometer (MODIS) images and National Oceanic Atmospheric Administration (NOAA) Interactive Multisensor Snow and Ice Mapping System (IMS) snow and ice charts. The obtained correlation coefficients with IMS charts for 2007 and 2008 were 0.92 and 0.83, respectively. The technique has been proposed as one of the candidate ice-mapping techniques for the future Geostationary Operational Environmental Satellite-R Series (GOES-R) Advance Baseline Imager (ABI) instrument.

1. Introduction

Sea and lake ice presents an important weather and climate factor and a sensitive climate indicator. Information on the ice extent and concentration, along with information on their long-term trends is needed in a large number of research and operational applications, including, in particular, numerical weather prediction, climate-change studies, transportation, oil exploration and extraction, ecology, biochemistry and biology.

In the last 30 years, the vast majority of data on ice distribution and variation was obtained using satellite remote-sensing techniques. Large area coverage and frequent repeat cycles make satellite observations an effective tool for ice-cover observation and monitoring. When selecting a particular type of satellite data for ice monitoring, most often the choice is made in favour of observations in the passive microwave band. These observations are practically weather independent, do not require daylight and are relatively easy to interpret. In previous studies, data from various passive microwave sensors have been successfully used to assess both regional and global

*Corresponding author. Email: temimi@ce.ccny.cuny.edu

International Journal of Remote Sensing
ISSN 0143-1161 print/ISSN 1366-5901 online
http://www.tandf.co.uk/journals
DOI: 10.1080/01431160903578820

changes in sea-ice extent and concentration (Gloerson *et al.* 1990, Cavalieri *et al.* 1999, Comiso *et al.* 2003, Kern *et al.* 2003, Markus *et al.* 2006, Powell *et al.* 2006).

Active microwave images have also been used to obtain information on ice properties (Shokr 1990, Shokr *et al.* 1995). Their high spatial resolution and their capability to sense surface conditions at night and under cloudy conditions make them attractive for such applications. However, the main limitations of active microwave techniques are their relatively limited scene extent and long revisit time. A constellation of active microwave sensors would allow for repetitive large-scale ice analysis.

Another technique that is actively used for remote mapping and monitoring of ice distribution is based on satellite observations in the visible and infrared bands. Unlike microwave data, application of satellite observations in the visible and infrared is limited to daytime clear-sky conditions. Therefore, they are less effective in monitoring large masses of ice in the polar regions. However, their finer spatial resolution, of the order of 1 km or less, gives them an advantage over microwave data in mapping and monitoring ice cover over small inland water bodies, lakes and even some rivers. Visible and infrared data are also more effective in detecting ice along coastal lines. At passive microwave frequencies, coastal areas present a problem since the spectral response of a mixed land/water scene may be similar to that of ice.

All current ice-identification algorithms using observations from visible and infrared sensors have been applied to data from polar-orbiting satellites. Zibordi and Van Woert (1993), Zibordi *et al.* (1995), Key *et al.* (2001) and Xuanji and Key (2001, 2005) have used images of the Advanced Very High Resolution Radiometer (AVHRR) onboard the National Oceanic Atmospheric Administration (NOAA) polar-orbiting satellite to identify and map ice cover. Since 2000, ice mapping is routinely performed with data from the Moderate Resolution Imaging Spectroradiometer (MODIS) onboard the Terra and Aqua satellites (Riggs *et al.* 1999, Hall *et al.* 2004, Drue and Heinemann 2005).

Availability of observations in the visible, middle-infrared and infrared spectral bands from geostationary satellites makes them another potential source of information on ice cover and concentration. The primary advantage of geostationary satellites over polar-orbiting satellites consists of a much higher temporal frequency of observations. Frequent (15–30 minutes) observations from geostationary satellites give better chances to observe cloud-clear scenes during the day than with 1–2 observations per day available from polar-orbiting platforms. Frequent temporal coverage and high spatial resolution enable better tracking of ice motion. Note that the effective spatial resolution of geostationary data degrades at high latitudes because of the large viewing zenith angle. Despite this fact, the spatial resolution remains appropriate for ice mapping and monitoring.

In this study, we present a new algorithm for sea-ice identification and mapping based on observations in the visible and infrared wavelengths from geostationary satellites. The idea was to develop a technique that would make use of frequent observations from geostationary satellites. The algorithm has been developed and tested with data from Spinning Enhanced Visible and Infrared Imager (SEVIRI) onboard Meteosat Second Generation (MSG) satellites. The algorithm was applied to map and monitor ice cover over the Caspian Sea.

2. Study area and data

2.1 *Study area*

The Caspian Sea is located in western Asia on the eastern edges of Europe, landlocked between Azerbaijan, Iran, Kazakhstan, Russia and Turkmenistan (figure 1). The total

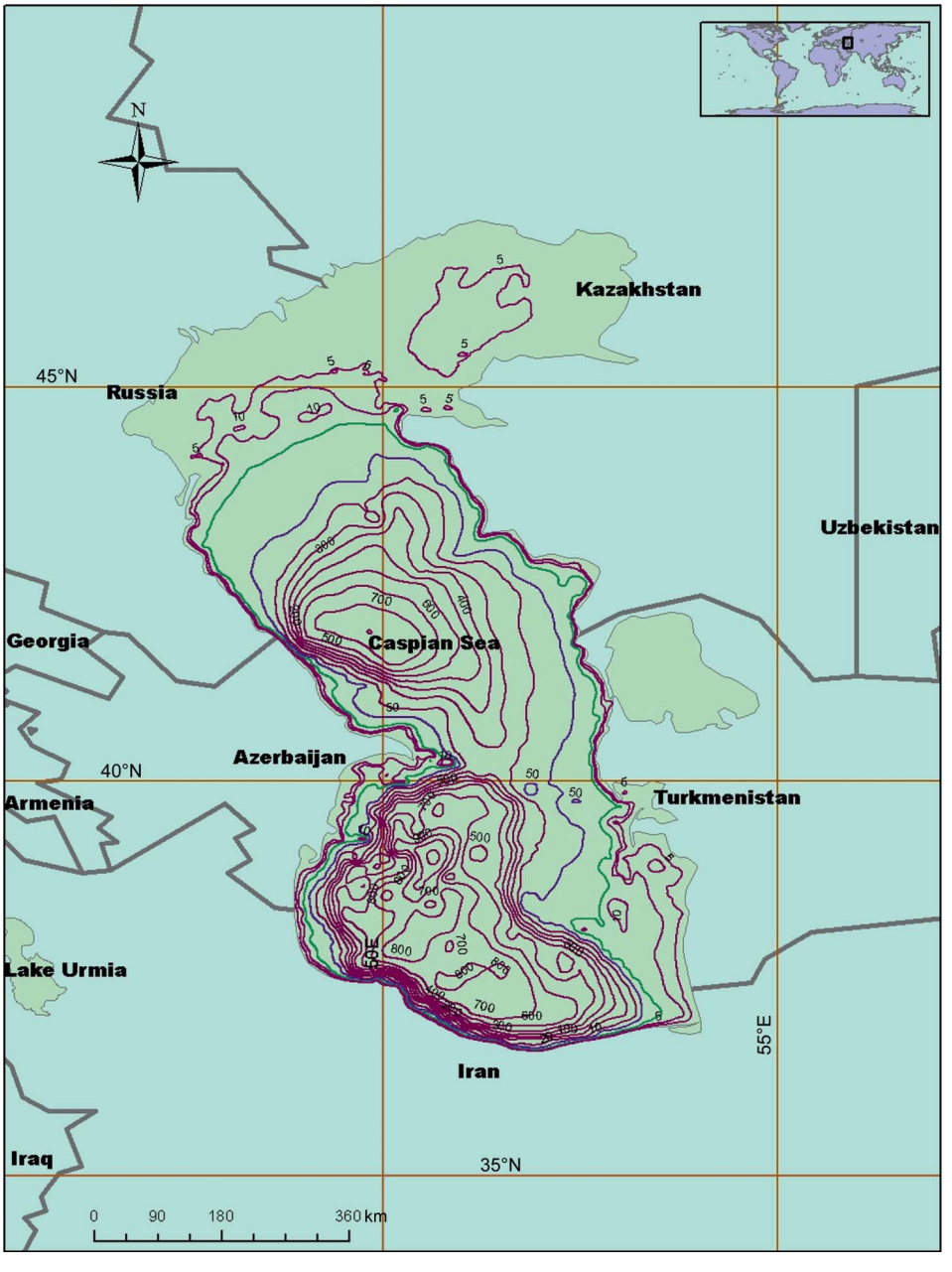

Figure 1. The Caspian Sea: location and bathymetry (see also Caspian Environment Programme (2008)).

area of the Caspian Sea is approximately 386 400 km^2, which makes it the largest completely enclosed body of salt water in the world. In winter, the northern part of the Caspian Sea freezes, with maximal ice extent ranging from 20 000 to around 95 000 km^2 (Kouraev *et al.* 2004b). During a severe winter season, a small amount of sea ice is

observed along the shoreline in the central and southern parts of the sea. The length of the ice-covered period depends on weather conditions and may exceed 4 months in the most northern locations. Ice melting starts typically in March and continues until early April. Ice pack in the north-eastern regions can reach 1 m thickness in the middle of winter season.

The Caspian Sea is completely covered by MSG SEVIRI data and therefore presents a relevant study site to develop and test MSG-based ice detection and mapping algorithms. There are indications that, in the last few years, the ice extent in the Caspian Sea has been gradually decreasing (Kouraev *et al.* 2003, 2004a). Therefore, establishing a routine ice-monitoring system for the Caspian Sea may help to better assess these trends and understand their causes. Information on ice-cover distribution and trends is also important for oil-drilling and -extraction activity in the eastern part of the sea.

2.2 *Data*

The SEVIRI is a 13-channel radiometer onboard MSG satellites. It performs full-disk observations in the visible to infrared spectral range at 15-minute intervals. The nominal spatial resolution at nadir ranges from 1 km for the high-resolution visible (HRV) channel data to 3 km for all other channel data. For this study, we have collected full-disk MSG SEVIRI data at 30-minute interval during the winter seasons of 2007 and 2008. The acquired data comprised measurements in channel (ch.) 1 (centred at 0.6 μm), ch. 2 (0.9 μm), ch. 3 (1.6 μm) and ch. 9 (11 μm). Observations in the reflective and thermal channels were converted correspondingly into reflectance normalized by the cosine of the solar zenith angle and into brightness temperature. SEVIRI data over the northern part of the Caspian Sea were extracted from the full-disk imagery and regridded to a latitude–longitude projection with 0.02° (or about 2 km) grid. The size of the grid corresponds to the effective spatial resolution of the HRV channel data over the Caspian Sea. At large viewing zenith angles, the effective spatial resolution of the data degrades. At a 65° zenith angle, the size of the instrument footprint on the ground is approximately twice as large as in nadir. Only daytime observations with a solar zenith angle above 80° are processed. Land-surface pixels have been masked out using the land-surface type dataset developed at the University of Maryland Department of Geography (Hansen *et al.* 1998).

For the validation of the ice-cover maps obtained, we have acquired daily snow and ice charts generated within NOAA Interactive Multisensor Snow and Ice Mapping System (IMS) (NOAA/NESDIS/OSDPD/SSD 2004). IMS snow charts are originally prepared on a polar-stereographic projection at the nominal spatial resolution of 4 km. The charts have been converted to the geographic projection of MSG images to make the two products easily comparable. Figure 2 presents an example of the IMS snow and ice chart over the Caspian Sea study area.

3. Spectral features of ice, water and clouds

Similar to snow, the reflectance of thick ice is very high in the visible band, but drops substantially in the shortwave and middle-infrared bands (Comiso and Steffen 2001). This specific spectral signature is different from spectral signatures of water and most types of clouds, and therefore provides the physical basis for ice identification from space. In practice, however, satellite-observed scenes present a mixture of two or three surface categories (ice, water, clouds) that substantially complicates their

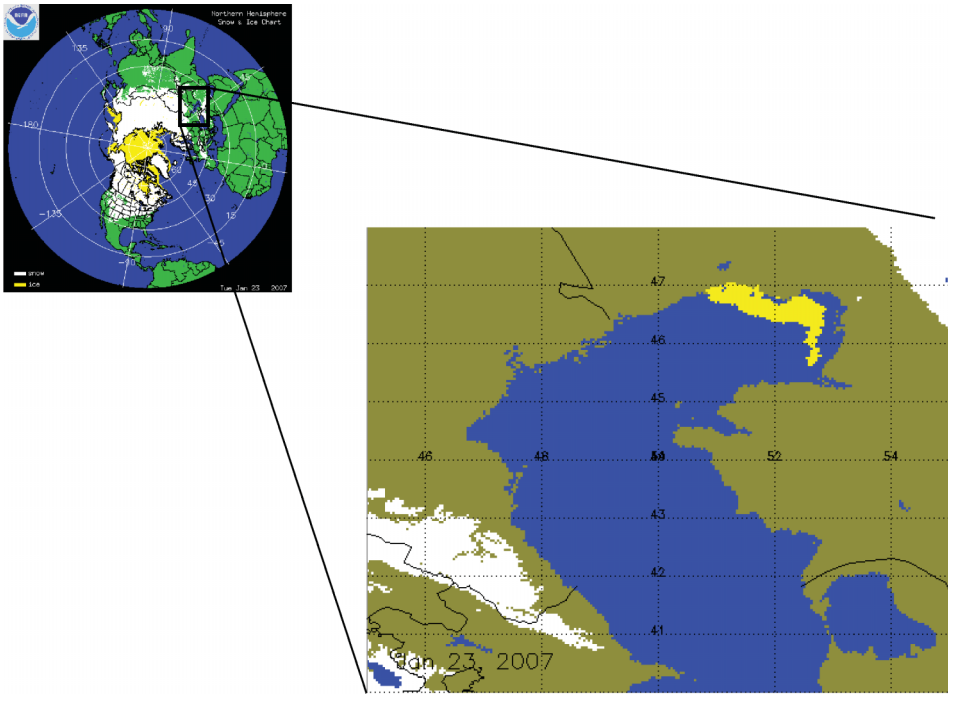

Figure 2. Example of NOAA IMS northern hemisphere snow/ice charts and the portion of the product over Caspian Sea in latitude–longitude projection on 23 January 2007. In the charts, snow is white and ice is yellow.

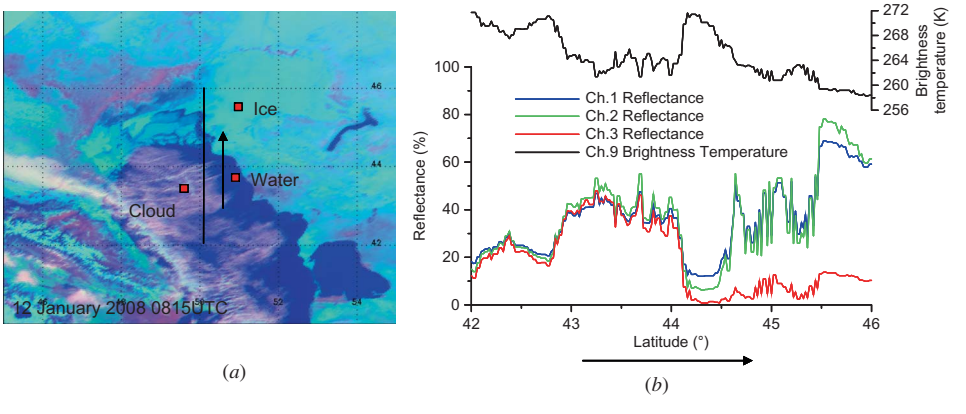

(*a*) (*b*)

Figure 3. (*a*) False-colour (RGB) SEVIRI image over the Caspian Sea taken on 12 January 2008 0815 Coordinated Universal Time (UTC) and (*b*) reflectance and temperature values along the image cross section (black line in (*a*)).

classification. The graphs in figure 3 present SEVIRI observations along a cross section in the Caspian Sea and give an idea about reflectance values and spectral reflectance patterns corresponding to different surface-cover types. Clouds of variable thickness over ice-free water in the southern portion of the cross section (42°–44° N)

result in high, up to 80%, reflectance values and cause their high spatial variability. Reflectance values in all three spectral bands, visible (ch. 1), near-infrared (ch. 2) and shortwave infrared (ch. 3) are close and are negatively correlated with infrared brightness temperature. Ice-free and cloud-clear water at around 44.3° N causes the reflectance to drop. The infrared brightness temperature observed in SEVIRI ch. 9 (11 μm) in this part of the cross section is about 272 K and exceeds the sea-water freezing point. The increase in the reflectance and decrease in the infrared brightness temperature from 44.5° to 45.5° N is apparently due to a gradual increase in the concentration of ice northward. Increase in the reflectance is the largest in the visible and near-infrared bands, whereas, even for thick ice in the northern portion of the cross section, the reflectance in the shortwave infrared remains at about 10%.

Due to high satellite and solar zenith angles corresponding to SEVIRI wintertime observations over the Caspian Sea, atmospheric effects in the observed reflectance may be substantial. In the SEVIRI full-disk image, the Caspian Sea is located near the edge of the scan (figure 4) and is observed from the MSG images at large satellite zenith angles, 65°–70°. Atmospheric scattering and absorption generally increase the satellite-observed reflectance over dark surfaces and decrease it over very bright surfaces. Because of larger atmospheric contributions at shorter wavelengths, the contrast between ice-free water and ice is more pronounced in the near-infrared (SEVIRI ch. 2) than in the visible spectral band (ch. 1). Therefore, application of SEVIRI observations in ch. 2 for mapping ice appears preferable.

Reflectances observed in all spectral bands in cloud-clear portions of the SEVIRI imagery over the Caspian Sea exhibit strong angular anisotropy (see figure 5). This fact has to be accounted for in the development of the image-classification algorithm. Over

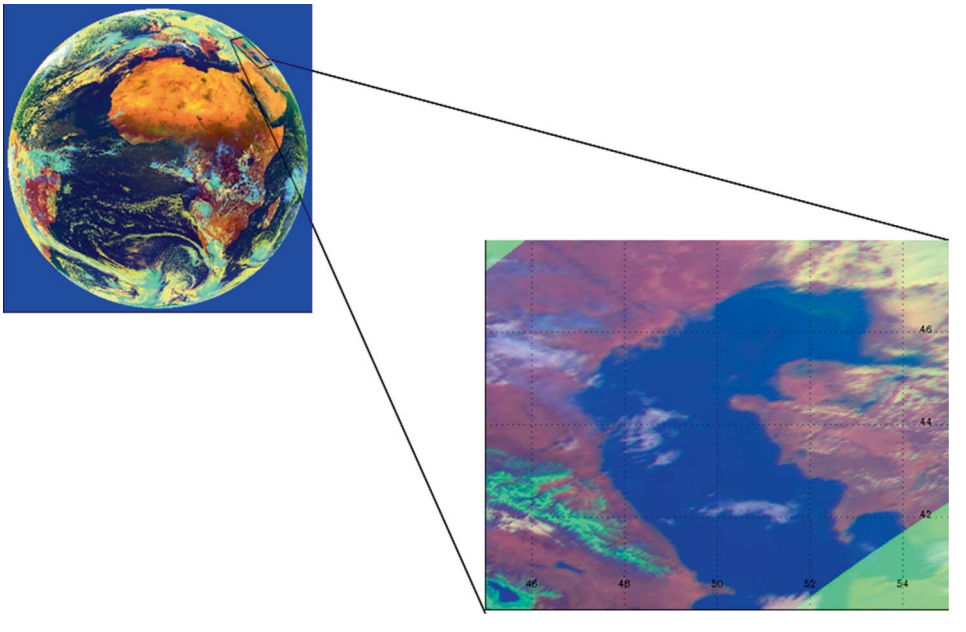

Figure 4. MSG SEVIRI full-disk false-colour composited (RGB) image and the portion of the image over Caspian Sea reprojected to latitude–longitude grid on 23 January 2007 at 10 h 15 m AM UTC.

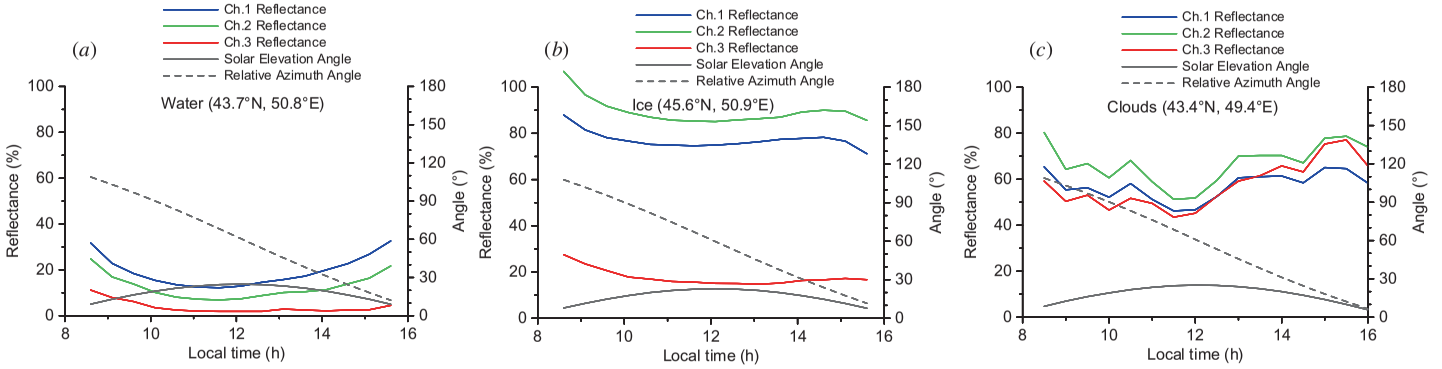

Figure 5. Diurnal change of spectral reflectance in SEVIRI ch.1 (0.6 μm), ch. 2 (0.8 μm) and ch. 3 (1.6 μm) for: (*a*) cloud-clear water, (*b*) cloud-clear ice and (*c*) a cloudy scene. Locations of 'water', 'ice' and 'cloudy' sites are shown on the image in figure 3(*a*).

dark surfaces (e.g. open water or water with a small concentration of ice), atmospheric scattering typically causes the reflectance to increase at low solar elevation angles. As a result, the SEVIRI reflectance over water (figure 5(*a*)) is larger both in the morning and in the evening. Over thick ice, the observed reflectance substantially increases at low solar elevation angles only in the forward scattering direction (azimuth angles over 90°). In the backscatter, low reflectances of ice may even cause a drop in the observed top of the atmosphere reflectance in the visible and near infrared spectral bands (figure 5(*b*)). The presence of clouds in the instrument field of view causes a considerable temporal variation of the scene spectral response. There is an indication of some angular dependence in the reflectance of the cloudy scene (figure 5(*c*)), however large temporal variation of the reflectance associated with the cloud movement prevents us from examining this feature.

4. Ice-mapping algorithm and data-processing system

The developed ice-mapping algorithm uses all available half-hourly daytime SEVIRI images to generate instantaneous, image-based ice maps, as well as composited ice products on a daily basis. The algorithm is completely automated. It consists of several steps, which include cloud identification, ice/water separation, estimation of the ice fraction and product compositing (see the flow chart in figure 6). A detailed description of every step of the procedure is given below.

4.1 *Cloud detection*

Identification of clouds in satellite images is performed with a threshold-based algorithm using observations in the shortwave infrared spectral band (1.6 μm, SEVIRI

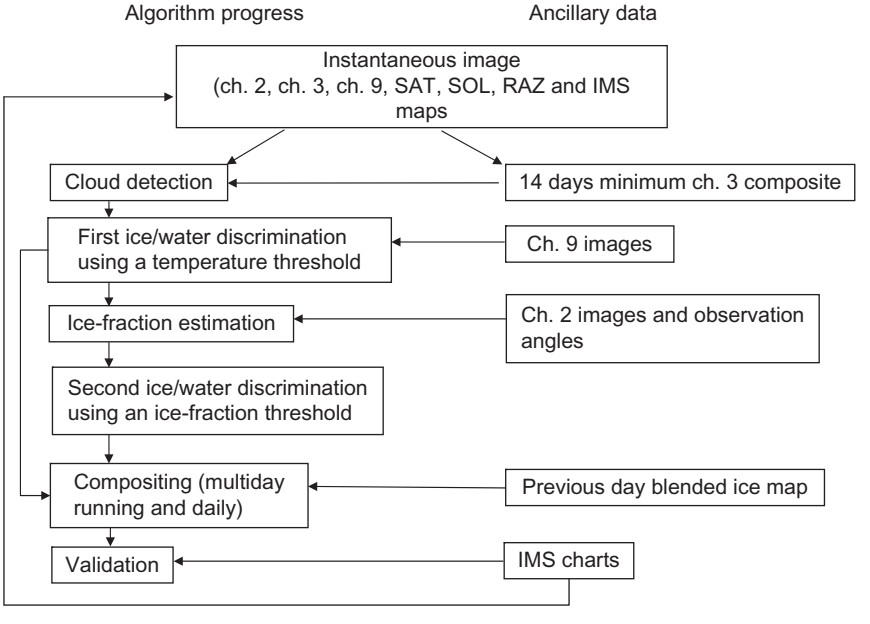

Figure 6. Flowchart of the algorithm. SAT, satellite zenith angle; SOL, solar zenith angle; RAZ, relative azimuth.

ch. 3). In this spectral band, the reflectance of most clouds exceeds the reflectance of both ice and water.

Due to a noticeable dependence of satellite-observed reflectance of ice and water on the viewing and illumination geometry of observations, application of the same fixed threshold value to separate clear and cloudy observations in all images acquired during the day leads to misclassifications. To improve the classification accuracy, we have developed a dynamic system that establishes location-dependent threshold values for every image acquisition time. Within this system, for every SEVIRI acquisition time, we composite all images acquired during the previous 2-week period. The compositing procedure retains observation with the smallest reflectance in SEVIRI ch. 3. As a result, the composited image contains a much larger portion of cloud-clear observations than any instantaneous images obtained during the day. The remaining cloudy observations are distinguished from cloud-clear measurements by examining the diurnal change of composited reflectances in every pixel. Excessive temporal variation of the observed reflectance is indicative of clouds. Cloudy observations are identified and are replaced in the composited images by predicted cloud-clear reflectance values by applying quadratic interpolation to the diurnal reflectance time series. The quadratic interpolation between the 14 lowest reflectances in ch. 3 determined through the composting procedure is necessary to account for persistent cloudy conditions during the composting period (i.e. 14 days) and therefore higher values of reflectance in ch. 3. The quadratic interpolation eliminates this possible outlier and ensures a typical and smooth appearance of the diurnal reflectance time series.

To account for possible inaccuracies in predicted values of the cloud-clear shortwave infrared reflectance and for possible variations in the ice concentration during the 14-day period, we set up the threshold value separating cloud-clear and cloudy scenes at the level exceeding by 10% the ch. 3 cloud-clear reflectance determined through the compositing procedure.

4.2 *Ice identification and ice-fraction estimation*

At the ice-identification stage, a two-step algorithm is applied to split all cloud-clear pixels into ice-covered and ice-free categories. A preliminary separation between ice-covered and ice-free pixels is performed by the value of the brightness temperature observed in the SEVIRI 11 μm infrared window channel (ch. 9). The threshold value separating clear water and pixels that may contain ice was set equal to 274 K. This threshold was set above the sea-water freezing temperature to avoid any possible misclassification of water pixels as ice. All remaining pixels are processed subsequently so they can be classified as ice or water.

At the second step, pixels identified as potentially ice covered are further processed to estimate the ice fraction. Ice fraction was calculated with a linear-mixture technique using the reflectance observed in the SEVIRI near-infrared spectral band (ch. 2):

$$F = \frac{R_{\text{obs}} - R_{\text{water}}}{R_{\text{ice}} - R_{\text{water}}}, \tag{1}$$

where R_{obs} is the observed reflectance of the scene, R_{water} and R_{ice} are the reflectance of end-members representing ice-free water and ice, respectively.

To reduce the risk of possible misclassifications, we have labelled pixels with ice concentration above 30% as 'confirmed' ice, whereas pixels with lower ice concentration were labelled as clear water. The threshold value of 30% corresponds to the

World Meteorological Organization guidelines (WMO 1970), where ice concentrations under 30% are considered as a mix of water and very open ice. A similar approach is also adopted by Williams *et al.* (2002).

There is a strong angular anisotropy inherent to satellite-observed reflectance in the visible and near-infrared spectral bands. Therefore, when calculating the ice fraction, it is important to bring all reflectances in formula (1) to the same geometry of observations. In this study, we have normalized R_{water} and R_{ice} to the current geometry of observations (corresponding to R_{obs}) using Artificial Neural Networks (ANNs). A multilayer perceptron neural network trained by the backpropagation algorithm was used in this study. The backpropagation technique (or generalized delta rule) presented by Rumelhart *et al.* (1986) has been largely used in training algorithms in remote sensing, as well as in a wide range of neural-network applications.

The network uses values of three angles (satellite zenith angle (SAT), solar zenith angle (SOL) and the relative azimuth (RAZ)) as an input, and generates one output value presenting the predicted reflectance for the given geometry of observations. To perform the network training and validation, we collected a dataset of satellite observations over cloud-clear water and cloud-clear thick ice. Observations were selected through interactive visual analysis of satellite imagery. The dataset included over 10 000 samples of data corresponding to clear water and over 4000 observations of ice. When collecting the dataset, we tried to evenly cover the whole range of possible geometries of observations and to equally represent all areas of the north of the Caspian Sea. Training of the network was performed with more than half of the data in the dataset (7000 observations of water and 2500 observations of ice), whereas the rest of the data were used to test the accuracy of the model. The root-mean-square errors (RMSEs) of the predicted reflectances were equal to 3.2% and 4.8% for open water and ice-covered surfaces, respectively.

4.3 *Compositing approach and products*

All classified SEVIRI 30-minute images are further used in the compositing procedure to generate daily and multiday running composited ice maps. The daily compositing algorithm retains all cloud-free retrievals made during a day. If more than one cloud-free observation was available during the day, the algorithm selects the 'warmest' observation, i.e. the one having the highest infrared brightness temperature in ch. 9. The daily compositing, however, is not sufficient to completely remove all cloudy pixels and to generate a continuous ice-distribution map. Therefore, an additional running composited map has been developed. The latter map is composed of the latest available cloud-free retrieval for every pixel. In the processing system, the running composited map is initialized with the IMS map for the first day and then corrected with SEVIRI-based ice retrievals. The running composite map is therefore completely cloud free.

5. Results and discussion

The developed approach has been applied to MSG SEVIRI imagery acquired at 30-minute interval during the winter seasons of 2007 and 2008. As an example of the derived instantaneous ice product, figure 7 presents the ice-concentration map obtained on 28 February 2007 at 11 h 15 m AM UTC. The distribution of ice concentration in the northern portion of the Caspian Sea mapped in the

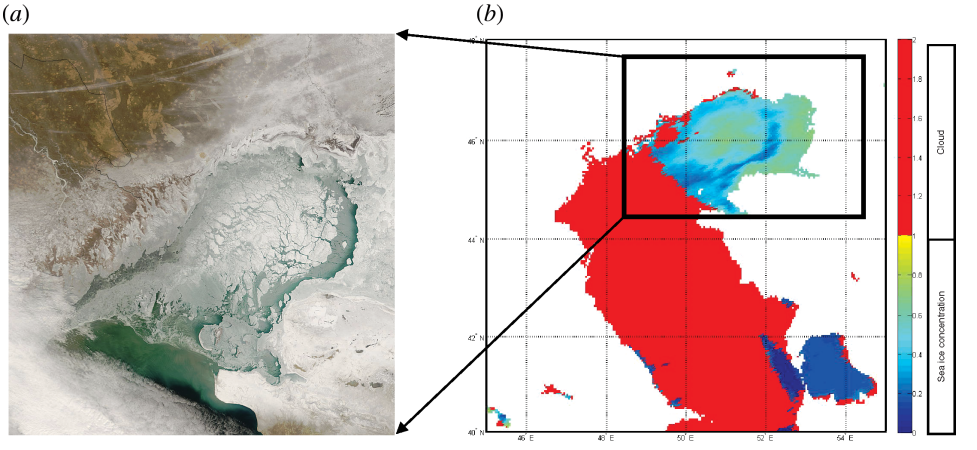

Figure 7. (*a*) SEVIRI-based sea-ice map over the northern part of the Caspian Sea on 28 February 2007 at 11 h 15 m AM UTC and (*b*) the MODIS true-colour image for the same day.

MSG-based product agrees quite well with the distribution of ice that is seen in the MODIS image for the same day (see figure 7). In particular, both images show ice-free pixels along the northern shoreline of the Caspian Sea. Shallow water in the northern part of the sea, as presented in figure 1, is more favourable for the presence of ice. In both images, the ice concentration increases towards the centre of the northern region of the sea.

A series of instantaneous ice maps and corresponding false-colour satellite images acquired at different times of the same day is presented in figure 8. Qualitative comparison of derived maps with the imagery demonstrates a high accuracy of cloud identification. The derived maps also show a small increase of the ice extent in the northern part of the Caspian Sea in the late afternoon. This increase is most probably spurious.

As compared to instantaneous images, the daily composited map provides better effective area coverage due to reduced cloud contamination. The reduction in the cloud amount due to compositing can be easily seen from the comparison of instantaneous ice maps in figure 8 and the daily composited ice map for the same day. To quantitatively evaluate the effect of cloud-cover reduction, we have calculated the cloud amount in daily composited ice maps and in ice maps derived from instantaneous satellite images. The percent cloud reduction has been calculated as:

$$\text{Cloud\_reduction} = 1 - \left(\frac{\text{Cloud}_{\text{dc}}}{\text{Cloud}_{\text{inst}}}\right), \tag{2}$$

where Cloud_{dc} is the cloud extent in the daily composited image and $\text{Cloud}_{\text{inst}}$ is the cloud extent in the ice map derived from instantaneous images. In this study, we have compared the cloud amount in daily composited images with cloud amount in instantaneous images taken at 10 h 45 m and at 13 h 45 m local time. The average percent cloud reduction ranged from 22% to 25% for these two times for the winter seasons of 2007 and 2008. On some days, the reduction has reached 50%. The times of 10 h 45 m and 13 h 45 m correspond to overpass times of the Terra and Aqua satellites with MODIS instruments onboard. Therefore, the results presented above

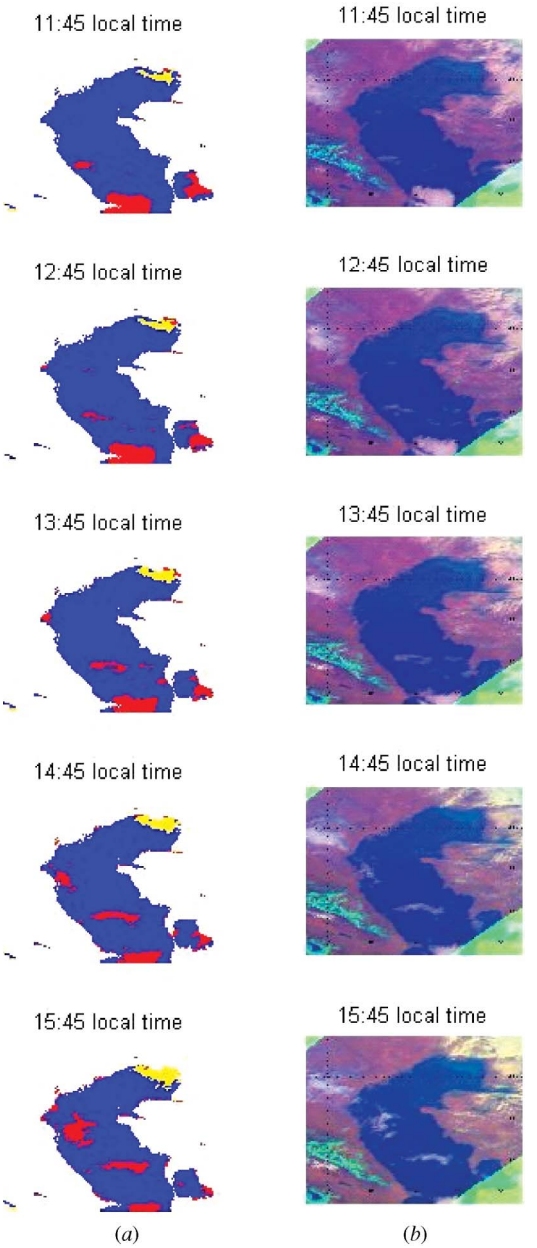

Figure 8. (*a*) Instantaneous ice maps (cloud in red, water in blue and ice in yellow) and (*b*) original MSG SEVIRI images on 23 January 2007. False-colour images in (*b*) are constructed with ch. 3 reflectance (red), HRV reflectance (green) and inverted infrared brightness temperature (blue).

characterize the expected reduction of the cloud cover in the geostationary satellite ice product as compared to the one based on polar-orbiting satellite data.

The performance of the image classification and ice-mapping algorithm has been assessed by comparing the total ice extent obtained to the one derived from the IMS charts. The results presented in figure 9 demonstrate the agreement between the sea-ice surface area estimated from the two products during the 2007 and 2008 winter seasons. Only cloud-free pixels in daily composited images have been considered in the comparison. The obtained correlation coefficients for 2007 and 2008 were 0.92 and 0.83, respectively.

The multiday running composite eliminates all clouds and thus delivers a continuous ice-distribution map. Figure 10 compares daily and running composites obtained on 23 January 2007 with the corresponding IMS chart. All images present a similar ice-distribution pattern in the northern part of the sea.

In order to assess the accuracy of the running composite ice map, we have calculated the Probability of Detection (POD) of ice and water for all daily maps obtained during the two winter seasons. Following Marzban (1998) and Williams *et al.* (2002), the POD was defined as:

$$\mathrm{POD} = \frac{A}{A + C}, \tag{3}$$

where A is the number of pixels that belong to a certain class X and have been correctly classified as X; C is the number of pixels that belong to class X, but have not been identified as X.

Ice and water POD values in table 1 show that, except for the ice detection in 2007, the POD was equal to or exceeded 80%. Clear water was detected with better accuracy than ice. The latter can be explained by the fact that most clear-water pixels are warmer than cloud and ice. Therefore, they are better identified using the infrared brightness-temperature threshold test. Part of the disagreement between IMS charts and running composite maps can be attributed to inertia inherent to the automated product. Quite often, IMS analysts can see the sea surface through semitransparent clouds and update the ice map if necessary. For the automated algorithm, any cloud

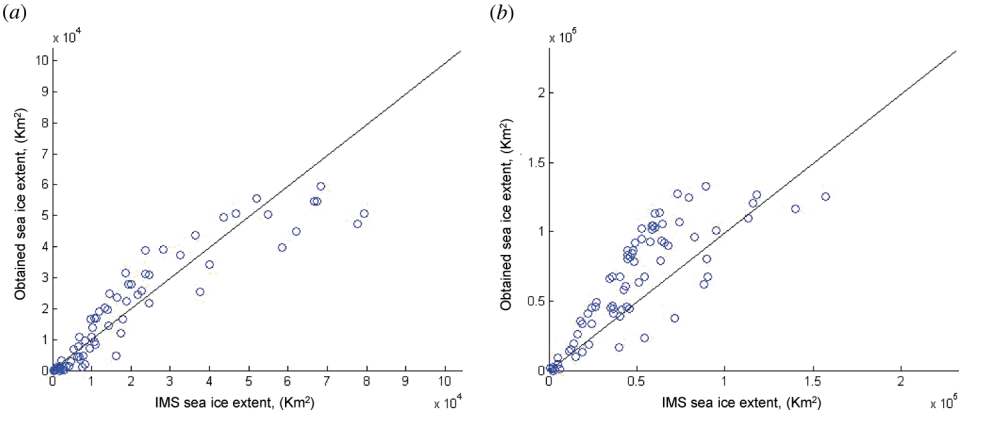

Figure 9. Scatter plots of the sea-ice extent in the Caspian Sea estimated from MSG SEVIRI blended ice maps and from IMS charts in (*a*) 2007 and (*b*) 2008.

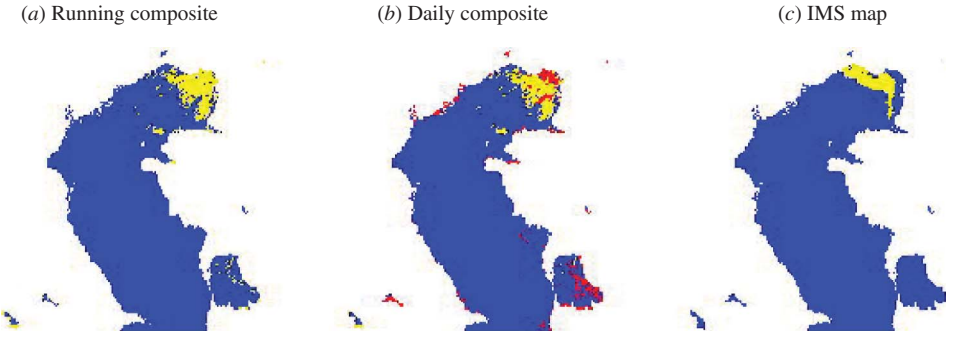

Figure 10. (*a*) Running and (*b*) daily composited ice maps for 23 January 2007. (*c*) IMS ice chart for the same day. In the three images cloud is in red, water in blue and ice in yellow.

Table 1. Average POD values for ice and water classes obtained in 2007 and 2008.

	Class	
	Ice%	Water%
2007	64	94
2008	80	89

prevents updating of the running composited map and therefore causes a delay in reproducing the changes in the ice extent and distribution.

Seasonal variation of the total ice extent determined was also assessed and validated using the IMS charts. Figure 11 compares time series of the sea-ice extent derived from IMS maps and from multiday running composite ice maps in 2007 and 2008. The obtained sea-ice values compare well with those determined from the IMS. The agreement, particularly in 2008, is better in the middle of the winter. In the beginning of winter 2008, the time series of SEVIRI-based ice extent show significant fluctuations. This happens because of the adjusting cloud-detection threshold, which leads to a misclassification of cloudy pixels during the first days of the simulation. The threshold stabilizes later, and fluctuations become less significant.

Towards the end of the month of February, IMS values, in 2007 and 2008, are slightly higher. The time series of sea-ice extent show a gradual decrease of the ice cover in early spring (early March) marking the start of the ice breakup. In 2007, the ice breakup was preceded by a rapid increase in total ice surface area. However, in 2008, the ice extent was stable prior to the start of the breakup. The ice breakup started almost at the same time, i.e. late February, in 2007 and 2008, despite the difference in preceding conditions.

Underestimation of the total sea-ice extent in early March, 2007 and 2008, with respect to IMS values can be explained by the change in ice-cover properties at the end of the winter season. Dark melting broken ice with a concentration below 30% may still be mapped by IMS analysts, whereas these pixels are systematically classified as open water by the automated algorithm. The adoption of gradually decreasing the ice-fraction threshold from 30% at the beginning of the winter season to 15% at its end

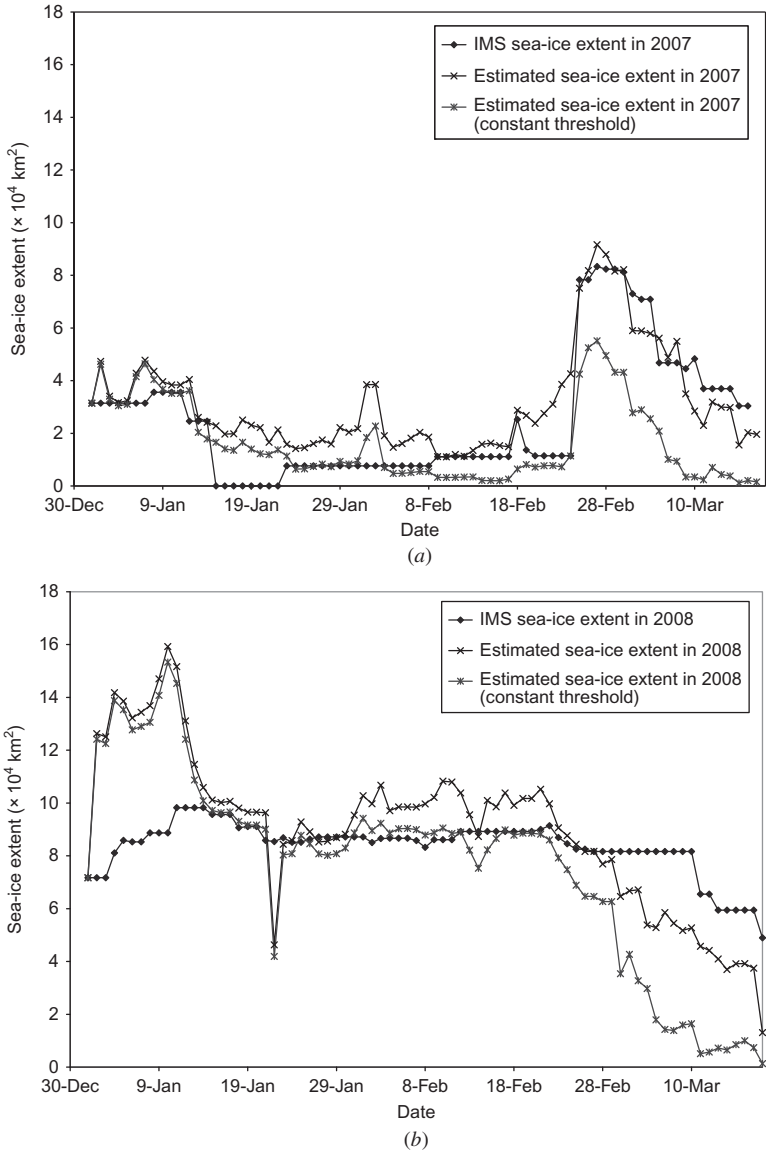

Figure 11. Sea-ice extent derived from IMS charts and from blended MSG SEVIRI maps in (*a*) 2007 and (*b*) 2008.

leads to more accurate ice mapping in spring, and thus substantially improves the correspondence between ice extent derived from SEVIRI data and from the IMS product (figure 11).

IMS charts are generated by analysts who visually inspect satellite images. The visual-inspection technique is subjective and does not systematically account for changes in ice concentration. So, pixels with an ice concentration lower than a predetermined threshold may be considered as ice pixels when delineating the ice extent visually. In addition, the graph of IMS sea-ice extent in figure 11 reveals consecutive plateaus, suggesting that over the Caspian Sea, the IMS charts are not

updated on a daily basis. This happens either when the analyst could not see the sea surface due to persistent cloud cover or when the change in the ice distribution since the previous day was insignificant. In the meantime, the ice extent is systematically updated because of the automated nature of the proposed approach. Also, short-term variations in the total IMS sea-ice extent can be seen in figure 11. For instance, in 2007, the total ice extent derived from IMS maps abruptly dropped from 2×10^4 km^2 on 14 January to 0 on 16 January. The total ice surface area, in IMS images, increased again on 23 January to reach 0.7×10^4 km^2. In contrast to the interactively derived maps, the automated approach demonstrates a gradual change of the ice extent between 14 January and 23 January 2007.

Recall that the cloud-detection algorithm is a threshold-based approach. The threshold is continuously updated. A constant value is added to the threshold to account for ice motion and surface-condition variation. Reducing the constant value added to ch. 3 minimum values makes the cloud detection more restrictive. However, it also increases the risk of misclassifying ice as thin cloud since they have a similar reflectance in ch. 3. The adopted constant value appears as a parsimonious compromise to appropriately detect cloudy pixels and also not confuse pure ice pixels with cloudy pixels.

The ANN used in this study to determine the end-members of the ice-fraction relationship has been trained using a large and representative sample of pixels selected manually over the Caspian Sea and covering different sun–satellite geometry conditions. The ANN has therefore been trained based on a set of various conditions in terms of ice concentration and geometry of observation. This makes the end-members determined to be more representative than a single typical reflectance of given class (whether it is water or ice). The adopted model is therefore flexible and adaptable to a variety of conditions.

The consideration of the sun–satellite geometry variation in this study makes the developed algorithm expandable in both space and time. The extension of the algorithm to the whole region in the northern hemisphere covered by SEVIRI and then by Geostationary Operational Environmental Satellite-R Series (GOES-R) will be investigated. The expansion to spring and summer seasons at higher latitude locations should be made with caution because of the temperature threshold. During freezing conditions (winter time), the gap between ice and water temperatures is significant (Meier 2005). Thermal channels in this case are suitable to discriminate between ice and open water. However, during the summer season, the thermal gap is reduced. In this case, the contrast between the reflectances of ice and water may be more appropriate to distinguish between the two classes. However, meteorological conditions can vary significantly throughout the season and considerably affect the pertinence of adopting the reflectance or temperature as a separator. Thus, a robust approach combining both reflectance and temperature should also be investigated in future work.

6. Conclusion

In this study, a new algorithm has been developed to generate maps of ice cover and ice fraction from observations of geostationary satellites. The algorithm makes use of multiple views per day available from geostationary satellites, and accounts for diurnal and seasonal changes in the viewing and solar illumination geometry of observations. The ice fraction is determined for every pixel within a linear-mixture approach from reflectance observed in the near-infrared spectral band. The end-

members of the linear-mixture model have been normalized to the same geometry of observations using ANNs. The network uses values of three angles as input, and generates one output value, presenting the predicted reflectance for the given geometry of observations.

All images acquired at 30-minute interval have been classified to identify ice, ice-free water and clouds. These instantaneous images have been further used to create daily and running composited ice maps. The daily compositing has minimized the cloud coverage, and the running compositing has generated completely cloud-free maps. The average cloud-coverage reduction because of the daily compositing process was over 25% with respect to the MODIS images acquired at the same overpass time.

Application of the algorithm to the Caspian Sea area has demonstrated its consistency and high accuracy of retrievals. The derived ice distribution corresponds well to the ice distribution mapped by NOAA analysts in the IMS charts. The agreement between the two products was 92% and 83% in 2007 and 2008, respectively. An underestimation of the ice extent in the IMS charts has been noticed in early March 2007 and 2008. This difference between the two products was caused by the decrease of ice concentration in this period marking the start of the ice meltdown. Dark melting broken ice with a concentration below 30% may be still mapped by IMS analysts, whereas these pixels are systematically classified as open water by the automated algorithm. An adjustable ice-concentration threshold has allowed the ice-concentration decrease to be accounted for and has therefore improved the agreement with IMS charts. Future work will investigate the expansion of the algorithm to entire full-disk images.

Acknowledgements

The authors would like to thank Dr Jeffry Key (NOAA/NESDIS in Madison) for his valuable comments and suggestions. Thanks also to anonymous reviewers for useful comments. This study was supported and monitored by the National Oceanic and Atmospheric Administration and GOES-R/AWG program under Grant NA08NES4280019. The views, opinions and findings contained in this report are those of the author(s) and should not be construed as an official National Oceanic and Atmospheric Administration or US Government position, policy or decision.

References

Caspian Environment Programme, 2008, Home page. Available online at: http://www.caspianenvironment.org (last accessed 12 January 2008). (Republic of Kazakhstan: CaspEco Project Management and Coordination Unit).

Cavalieri, D.J., Parkinson, C.L., Gloersen, P., Comiso, J.C. and Zwally, H.J., 1999, Deriving long-term time series of sea ice cover from satellite passive-microwave multisensor data sets. *Journal of Geophysical Research – Oceans*, **104**, pp. 15803–15814.

Comiso, J.C., Cavalieri, D.J. and Markus, T., 2003, Sea ice concentration, ice temperature, and snow depth using AMSR-E data. *IEEE Transactions on Geoscience and Remote Sensing*, **41**, pp. 243–252.

Comiso, J.C. and Steffen, K., 2001, Studies of Antarctic sea ice concentration from satellite data and their applications. *Journal of Geophysical Research*, **106**, pp. 31361–31385.

Drue, C. and Heinemann, G., 2005, Accuracy assessment of sea-ice concentrations from MODIS using in-situ measurements. *Remote Sensing of Environment*, **95**, pp. 139–149.

Gloerson, P., Cavalieri, D., Campbell, W.J. and Zwally, J., 1990, *Nimbus-7 SMMR Polar Radiances and Arctic and Antarctic Sea Ice Concentrations* (Boulder, CO: National Snow and Ice Data Center).

Hall, D.K., Key, J.R., Casey, K.A., Riggs, G.A. and Cavalieri, D.J., 2004, Sea ice surface temperature product from MODIS. *IEEE Transactions on Geoscience and Remote Sensing*, **42**, pp. 1076–1087.

Hansen, M.R., Defries, R.S., Townshend, J.R.G. and Sohlberg, R., 1998, *UMD Global Land Cover Classification, 1 Kilometer*, Department of Geography, University of Maryland, College Park, Maryland, 1981–1994.

Kern, S., Kaleschke, L. and Clausi, D.A., 2003, A comparison of two 85-GHz SSM/I ice concentration algorithms with AVHRR and ERS-2 SAR imagery. *IEEE Transactions on Geoscience and Remote Sensing*, **41**, pp. 2294–2306.

Key, J.R., Wang, X.J., Stoeve, J.C. and Fowler, C., 2001, Estimating the cloudy-sky albedo of sea ice and snow from space. *Journal of Geophysical Research – Atmospheres*, **106**, pp. 12489–12497.

Kouraev, A.V., Papa, F., Mognard, N.M., Buharizin, P.I., Cazenave, A., Cretaux, J.-F., Dozortseva, J. and Remy, F., 2003, *Variations of Sea Ice Extent in the Caspian and Aral Seas Derived From Combination of Active and Passive Satellite Microwave Data* (Toulouse, France: Institute of Electrical and Electronics Engineers Inc.).

Kouraev, A.V., Papa, F., Mognard, N.M., Buharizin, P.I., Cazenave, A., Cretaux, J.-F., Dozortseva, J. and Remy, F., 2004a, Sea ice cover in the Caspian and Aral Seas from historical and satellite data. *Journal of Marine Systems*, **47**, pp. 89–100.

Kouraev, A.V., Papa, F., Mognard, N.M., Buharizin, P.I., Cazenave, A., Cretaux, J.-F., Dozortseva, J. and Remy, F., 2004b, Synergy of active and passive satellite microwave data for the study of first-year sea ice in the Caspian and Aral Seas. *IEEE Transactions on Geoscience and Remote Sensing*, **42**, pp. 2170–2176.

Markus, T., Cavalieri, D.J., Gasiewski, A.J., Klein, M., Maslanik, J.A., Powell, D.C., Stankov, B.B., Stroeve, J.C. and Sturm, M., 2006, Microwave signatures of snow on sea ice: observations. *IEEE Transactions on Geoscience and Remote Sensing*, **44**, pp. 3081–3090.

Marzban, C., 1998, Scalar measures of performance in rare-event situations. *Weather and Forecasting*, **13**, pp. 753–763.

Meier, W.N., 2005, Comparison of passive microwave ice concentration algorithm retrievals with AVHRR imagery in arctic peripheral seas. *IEEE Transactions on Geoscience and Remote Sensing*, **43**, pp. 1324–1337.

NOAA/NESDIS/OSDPD/SSD, 2004, *IMS Daily Northern Hemisphere Snow and Ice Analysis at 4 km and 24 km Resolution* (Boulder, CO: National Snow and Ice Data Center).

Powell, D.C., Markus, T., Cavalieri, D.J., Gasiewski, A.J., Klein, M., Maslanik, J.A., Stroeve, J.C. and Sturm, M., 2006, Microwave signatures of snow on sea ice: modeling. *IEEE Transactions on Geoscience and Remote Sensing*, **44**, pp. 3091–3102.

Riggs, G.A., Hall, D.K. and Ackerman, S.A., 1999, Sea ice extent and classification mapping with the moderate resolution imaging spectroradiometer airborne simulator. *Remote Sensing of Environment*, **68**, pp. 152–163.

Rumelhart, D.E., Hinton, G.E. and Williams, R.J., 1986, *Learning Internal Representations by Error Propagation-Parallel Distributed Processing*, pp. 318–362 (Cambridge, MA: MIT Press).

Shokr, M.E., 1990, On sea-ice texture characterization from SAR images. *IEEE Transactions on Geoscience and Remote Sensing*, **28**, pp. 737–740.

Shokr, M.E., Wilson, L.J. and Surdu-Miller, D.L., 1995, Effect of radar parameters on sea ice tonal and textural signatures using multi-frequency polarimetric SAR data. *Photogrammetric Engineering and Remote Sensing*, **61**, p. 1463.

Williams, R.N., Michael, K.J., Pendlebury, S. and Crowther, P., 2002, An automated image analysis system for determining sea-ice concentration and cloud cover from AVHRR images of the Antarctic. *International Journal of Remote Sensing*, **23**, pp. 611–625.

WMO, 1970, *World Meteorological Organization Sea-ice Nomenclature – Terminology, Codes and Illustrated Glossary*, WMO/OMM/BMO-No. 259TP. 145, 4 (Geneva, Switzerland: WMO).

Xuanji, W. and Key, J.R., 2001, Spatial variability of the sea-ice radiation budget and its effect on aggregate-area fluxes. *Annals of Glaciology*, **33**, pp. 248–252.

Xuanji, W. and Key, J.R., 2005, Arctic surface, cloud, and radiation properties based on the AVHRR Polar Pathfinder dataset. Part II. Recent trends. *Journal of Climate*, **18**, pp. 2575–2593.

Zibordi, G. and Van Woert, M.L., 1993, Antarctic sea ice mapping using the AVHRR. *Remote Sensing of Environment*, **45**, pp. 155–163.

Zibordi, G., Van Woert, M., Meloni, G.P. and Canossi, I., 1995, Intercomparisons of sea ice concentration from SSM/I and AVHRR data of the Ross Sea. *Remote Sensing of Environment*, **53**, p. 145.